Photoionization using the XCHEM approach: Total and partial cross sections of Ne and resonance parameters above the $2s^2 2p^5$ threshold

Carlos Marante,[1] Markus Klinker,[1] Tor Kjellsson,[2] Eva Lindroth,[2] Jesús González-Vázquez,[1,*] Luca Argenti,[1,3] and Fernando Martín[1,4,5,†]

[1]*Departamento de Química, Módulo 13, Universidad Autónoma de Madrid, 28049 Madrid, Spain, EU*

[2]*Department of Physics, Stockholm University, AlbaNova University Center S-106 91, Stockholm, Sweden*

[3]*Department of Physics and CREOL College of Optics & Photonics, University of Central Florida, Orlando, Florida 32816, USA*

[4]*Instituto Madrileño de Estudios Avanzados en Nanociencia (IMDEA-Nanociencia), Cantoblanco, 28049 Madrid, Spain, EU*

[5]*Condensed Matther Physics Center (IFIMAC), Universidad Autónoma de Madrid, 28049 Madrid, Spain, EU*

(Received 5 May 2017; published 4 August 2017)

The XCHEM approach interfaces well established quantum chemistry packages with scattering numerical methods in order to describe single-ionization processes in atoms and molecules. This should allow one to describe electron correlation in the continuum at the same level of accuracy as quantum chemistry methods do for bound states. Here we have applied this method to study multichannel photoionization of Ne in the vicinity of the autoionizing states lying between the $2s^2 2p^5$ and $2s2p^6$ ionization thresholds. The calculated total photoionization cross sections are in very good agreement with the absolute measurement of Samson *et al.* [J. Electron Spectrosc. Relat. Phenom. **123**, 265 (2002)], and with independent benchmark calculations performed at the same level of theory. From these cross sections, we have extracted resonance positions, total autoionization widths, Fano profile parameters, and correlation parameters for the lowest three autoionizing states. The values of these parameters are in good agreement with those reported in earlier theoretical and experimental work. We have also evaluated β asymmetry parameter and partial photoionization cross sections and, from the latter, partial autoionization widths and Starace parameters for the same resonances, not yet available in the literature. Resonant features in the calculated β parameter are in good agreement with the experimental observations. We have found that the three lowest resonances preferentially decay into the $2p^{-1}\epsilon d$ continuum rather than into the $2p^{-1}\epsilon s$ one [Phys. Rev. A **89**, 043415 (2014)], in agreement with previous expectations, and that in the vicinity of the resonances the partial $2p^{-1}\epsilon s$ cross section can be larger than the $2p^{-1}\epsilon d$ one, in contrast with the accepted idea that the latter should amply dominate in the whole energy range. These results show the potential of the XCHEM approach to describe highly correlated process in the ionization continuum of many-electron systems, in particular molecules, for which the XCHEM code has been specifically designed.

DOI: 10.1103/PhysRevA.96.022507

I. INTRODUCTION

Over the past decades, the breakthroughs produced in the generation of ultrashort pulses in a broad range of the electromagnetic spectrum, from near-infrared (NIR) femtosecond pulses to extreme ultraviolet (XUV) and x-ray attosecond ones, have provided us with the tools to observe and control electron dynamics in a variety of different scenarios, relevant in physics, chemistry, and biology [1–9]. XUV and x-ray pulses are able to ionize atoms and molecules by absorption of a single photon. Therefore, the theoretical description of the dynamics induced by these pulses must explicitly account for the ionization continuum. In the case of intense pulses, like those obtained in x-ray free-electron lasers (XFEL) [10], the nonlinear dynamics generated by the absorption of several photons usually involves more ionization channels and implies that more than one electron can be promoted to the continuum.

Although a plethora of theoretical methods is available to accurately describe the ionization continuum of atoms (see, e.g., [11–15] and references therein), this is not the case for molecules, for which existing methods are usually designed to describe specific problems, usually in regions of the photoelectron spectrum where autoionization and electron correlation play a minor role. In contrast, for bound molecular states, electron correlation can be accurately handled by using a variety of quantum chemistry packages (QCP) based on *ab initio* methods [16–22]. With proper adjustments, these methods can also provide an accurate description of molecular resonances (hole, shake-up, and multiply excited states), for which electron correlation is even more important [23–26]. So, extending the applicability of these codes to the ionization continuum of molecules seems the natural way to proceed in order to get a similar good description of electron correlation in the continuum region of the molecular spectrum. However, in general, this is a very challenging task. Indeed, most QCPs make use of Gaussian or Slater-type basis functions centered on the various atomic locations, which is advantageous to accelerate convergence in comparison with single-center expansions but turns into a serious disadvantage when dealing with the electronic continuum. This is because Gaussian and Slater-type functions decrease exponentially and therefore are not appropriate to describe the oscillatory behavior of the continuum wave function in the asymptotic region (which is essential to impose the proper boundary conditions of scattering states). The problem cannot be solved by just increasing the number of basis functions, since this procedure rapidly runs into linear dependencies, thus allowing for the description of typically no more than one or two radial

*jesus.gonzalezv@uam.es
†fernando.martin@uam.es

oscillations [27–30]. For Gaussian functions, the standard in most QCPs due to their easiness for the evaluation of multicenter two-electron integrals, the situation is worse than for Slater functions, since they decrease more rapidly.

Previous work [31–36] has shown that continuum states of simple diatomic molecules can be accurately described by using more appropriate functions, such as B-splines [33,37,38] or finite-element discrete-variable-representation functions (FE-DVR) [39]. However, extension of these methods to larger molecules would be very involved, since, e.g., an efficient evaluation of bielectronic integrals and consideration of molecular symmetry would require the implementation of new algorithms, mimicking the path that standard QCPs have followed for decades. Thus most solutions proposed in the literature have adopted a more pragmatical approach, which is to combine existing QCPs with scattering methods that incorporate the latter basis functions. For instance, recently proposed methods complement the short-range part represented by Gaussian functions with a finite element (FE) representation of the radial coordinate [40,41], or a discrete variable representation (DVR) [42–46], or even plane waves [47]. Others just get rid of all exponentially decreasing functions by fitting them to a multicenter B-spline expansion and adding additional B-splines for the continuum part [48]. In a recent work [49], some of us have introduced the XCHEM approach, which overcomes the aforementioned limitations by combining state-of-the-art techniques for the calculation of correlated excited states, as implemented in MOLCAS and MOLPRO packages [17,50], with a single-center hybrid Gaussian and B-spline basis (GABS) for the description of the electronic continuum [51]. The performance of the method has been checked in helium and the hydrogen molecule [49]. An appealing feature of the XCHEM method is that it minimizes the number of mixed polycentric integrals (involving Gaussian and B-spline functions simultaneously) that is necessary to evaluate, so that the increase of computational effort when the number of electrons increases is comparable to that of conventional QCPs in bound-state calculations. Also, due to the hybrid nature of the GABS basis, increasing the size of the molecule from, let's say, N_2 to a small triatomic or tetra-atomic molecule, should keep computational cost almost at the same level. Although mainly designed to study molecular ionization, in this paper we have used the XCHEM method to study the resonant photoionization of the neon atom, the first truly polyelectronic system to which the method is ever applied. This is an important step to check its performance before moving to more complex targets.

The first unambiguous observations of resonant states in the photoionization spectra of noble gases were reported in the 1960s [52–55] and the unusual shape of the peaks observed in these experiments was explained by Fano in his seminal 1961 paper [56] as resulting from the interaction of a discrete state embedded in the continuum (see also [57]). Neon is the lightest noble atom in which the remaining cation has a truly polyelectronic character, so that photoionization dynamics is much richer than in helium. For this reason, neon has been systematically used to test new many-body theoretical methods. More recently, due to the recent advances in the generation of shorter and shorter pulses and the possibility to track electron wave-packet dynamics in real time, there has been a renewed interest in this system [58–62] that calls for additional theoretical effort.

In this paper, we have used the XCHEM method to describe the multichannel photoionization of Ne. We first compare with results of the well-established STOCK code [15] by performing calculations at the same level of theory and then with existing experimental and theoretical results. The good agreement with these results shows the good performance of the method. Then we report additional information not yet available in the literature, as partial photoionization cross sections, partial autoionization widths for the lowest three $^1P^o$ resonances converging to the $2s2p^6$ ionization threshold, and the corresponding Starace parameters [63] that control the line shapes of the resonance peaks observed in the partial photoionization cross sections. We show that, as assumed in earlier work, the $2s2p^6\epsilon d$ photoionization cross section generally dominates over the $2s2p^6\epsilon s$ one, but we now quantify the magnitude of this difference in a wide range of photon energies and found that, in the vicinity of the resonances, this is no longer the case.

The paper is organized as follows. Section II presents the theoretical background, with emphasis in the XCHEM approach and the theoretical method STOCK used for benchmarking. Section III illustrates the performance of XCHEM by using two different levels of electronic correlation and presents the results of the present work. The paper finishes with some conclusions and future perspectives in Sec. IV. Atomic units are used throughout unless otherwise stated.

II. THEORETICAL METHODS

When the Ne atom absorbs a photon from the radiation field, with a sufficiently high energy to eject an electron, the target ten-electron state $|i\rangle$ (usually the ground state) is transformed into one of the accessible nine-electron parent-ion states $|a\rangle$ plus an electron in the continuum with a given momentum $\vec{k}$ and spin projection σ:

$$\mathrm{Ne}_i + \gamma \rightarrow \mathrm{Ne}_a^+ + e_{\vec{k}\sigma}^- . \tag{1}$$

Although a single photon can lead to the ejection of more than one valence electron, due to electronic correlation, single ionization is by far the dominant process. The common practice in most theoretical approaches is to limit the Hilbert space to a subspace of configurations accounting for the most relevant dynamics of the photoionization problem. This can be realized by dividing the position space in two regions: an inner one, in which the target and parent-ion states lie, and an outer one, which contains the appropriate asymptotic solutions of the scattering states. The main differences among the available implementations based on this space partition lie in the theory level employed to compute the wave function in the inner part, and how it matches the long-range part of the wave function in the outer region. To compute the target and parent-ion states, any of the tools accounting for electron correlation in bound states can be used, e.g., multiconfiguration Hartree-Fock (MCHF), configuration interaction (CI), coupled cluster, etc. (see [64–66]). The next subsection summarizes the approach followed by XCHEM and how it has been implemented to study photoionization of the Ne atom. A more detailed description of the method can be found in Ref. [49].

A. XCHEM approach

We first define two radial ranges: a short range, $r_i < R_0$, where all N electrons are within a fixed radius R_0 from the center of mass of the parent ion and a long range, $r_N > R_0$, where one and only one electron (e.g., the Nth one) is allowed to be beyond R_0, that is $r_{i<N} < R_0$. The complete scattering function can be expressed in terms of a close-coupling (CC) expansion in terms of short-range N-electron states $\aleph_i$ and "extended" channel functions $\bar{\Upsilon}_{\beta i}$ [49]:

$$\Psi^-_{\alpha E} = \sum_i \aleph_i c_{i,\alpha E} + \sum_\beta \sum_i \bar{\Upsilon}_{\beta i} c_{\beta i,\alpha E}. \tag{2}$$

The extended channel functions $\bar{\Upsilon}_{\beta i}$ are defined as

$$\bar{\Upsilon}_{\beta i} = N_{\beta i}\, \hat{\mathcal{A}}\, \Upsilon_\beta(\mathbf{x}_1,\ldots,\mathbf{x}_{N-1};\hat{r}_N,\zeta_{N_e})\, \varphi_i(r_N), \tag{3}$$

where φ_i are radial functions suitable to describe the continuum, $N_{\beta i}$ are normalization factors ensuring the correct asymptotic behavior, and $\hat{\mathcal{A}}$ is the antisymmetrization operator. The asymptotically decoupled channel functions, $\Upsilon_\beta(\mathbf{x}_1,\ldots,\mathbf{x}_{N-1};\hat{r}_N,\zeta_N)$, are obtained by coupling the antisymmetrized parent-ion wave function Φ_b with the N-electron spin wave function χ, while its angular part, given by a symmetry adapted spherical harmonics $X_{\ell m}(\hat{r})$ [67], is factorized,

$$\begin{aligned}
&\Upsilon_\beta(\mathbf{x}_1,\ldots,\mathbf{x}_{N-1};\hat{r}_N,\zeta_N)\\
&\quad = {}^{2S+1}[\Phi_b(\mathbf{x}_1,\ldots,\mathbf{x}_{N-1}) \otimes^2 \chi(\zeta_N)]_\Sigma\, X_{\ell m}(\hat{r}_N)\\
&\quad = \sum_{\Sigma_b\sigma} C^{S\Sigma}_{S_b\Sigma_b,\frac{1}{2}\sigma}\, {}^{2S_b+1}\Phi_{b,\Sigma_b}\, {}^2\chi_\sigma(\zeta_N)\; X_{\ell m}(\hat{r}_N),
\end{aligned} \tag{4}$$

where $\mathbf{x}_i$ denotes the position and spin coordinates of electron i, $\hat{r}_N$ represents the angular coordinates of electron N, ζ_N is the spin component of electron N, S is the total spin of the system, Σ its z projection, S_b and Σ_b are the corresponding values for the parent ion, σ is the z component of the electron spin, and $C^{S\Sigma_b}_{S_b\Sigma_b,\frac{1}{2}\sigma}$ is a Clebsh-Gordan coefficient. The channel index β corresponds to the set of indexes (S,Σ,b,ℓ,m), while the parent-ion index b defines entirely the state of the parent ion, except for its total spin projection. As we will deal with spin-free Hamiltonians, the total spin S and the spin projection Σ are conserved. The $X_{\ell m}$ angular functions allow us to exploit the symmetry of the system, reducing the Hilbert space dimension considerably.

As the eigenstates of the parent ion (Φ_b) are negligible in the region $r_i > R_0$, the complete scattering wave function beyond that boundary can be written

$$\begin{aligned}
&\Psi^-_{\alpha E}(\mathbf{x}_1,\ldots,\mathbf{x}_N)\\
&\quad = \frac{1}{N}\sum_\beta N_{\beta E}\Upsilon_\beta(\mathbf{x}_1,\ldots,\mathbf{x}_{N-1};\hat{r}_N,\zeta_N)\frac{u^-_{\beta,\alpha E}(r_N)}{r_N},
\end{aligned} \tag{5}$$

where $u^-_{\beta,\alpha E}(r)$ is the radial function that describes the continuum electron, given asymptotically by

$$u^-_{\beta,\alpha E}(r) = \delta_{\alpha\beta}\sqrt{\frac{2}{\pi k_\alpha}}\, e^{i\Theta_\alpha(r)} - \sqrt{\frac{2}{\pi k_\beta}}\, e^{-i\Theta_\beta(r)}\mathbb{S}^*_{\beta\alpha}, \tag{6}$$

with

$$\Theta_\beta(r) = k_\beta r + \frac{Z}{k_\beta}\ln 2k_\beta r - \ell_\beta\pi/2 + \sigma_{\ell_\beta}(k_\beta), \tag{7}$$

where k_β is the absolute value of the momentum of the continuum electron in the β channel, Z the charge of the parent ion, σ_{l_β} the Coulomb phase, and $\mathbb{S}_{\alpha\beta}$ is the *on-shell* scattering matrix [68]. The incoming boundary conditions in Eq. (6) enforce the correct asymptotic behavior of the complete scattering wave function $\Psi^-_{\alpha E}$ for the photoionization process. The non-Coulomb phase shifts $\phi_\mu(E)$ are extra phases that appear in the scattering states due to the short-range non-Coulomb component of the interaction potential between the scattered electron and the target. That is why they are very sensitive to electron correlation and, thus, a good observable to assess the quality of the computed continuum. These phases can be obtained from the diagonalization of the $\mathbb{S}_{\beta\alpha}$ scattering matrix and are also known as eigenphases.

We use three different kinds of functions to build the N-electron basis: (i) a set of localized Gaussian functions $\{G^{MC}_i(\mathbf{x}_1)\}$ as provided by QCPs (for molecules, they would be located at the different atomic positions–multicenter expansion), (ii) a set of diffuse even-tempered Gaussian functions $\{G^{SC}_i(\mathbf{x}_1)\}$, and (iii) a set of B-spline functions $\{B_i(\mathbf{x}_1)\}$ starting at $r = R_0$. Basis functions defined in (ii) and (iii) constitute the so-called GABS basis, $\{G^{SC}_i(\mathbf{x}_1)\}\cup\{B_i(\mathbf{x}_1)\}$ (for molecules, these functions would be located at the center-of-mass–single-center expansion). The $G^{SC}_i(\mathbf{x}_1)$ functions are in principle defined in the whole interval $r\in[0,\infty)$; however, due to their fast exponential decrease, there is a distance R_1 ($R_1 > R_0$) beyond which the overlap with the B-splines starts to be negligible (see [51] for details). The region ($r\in[R_0,R_1]$) where both subsets overlap guarantees a smooth transition from the outer to the inner region, thus providing great flexibility to the $G^{SC}_i(\mathbf{x}_1)$ functions in the short-range region, because B-splines compensate the deficiencies of the $G^{SC}_i(\mathbf{x}_1)$ functions in reproducing the rapid oscillations of the diffuse states (Rydberg and continuum states). From R_1 on, B-splines take over the full description of the wave function. This is how the inner part of the space partition matches almost perfectly the outermost part, in contrast with methods that make use of a rigid boundary to divide the two regions [11]. The typical thickness of the $R_1 - R_0$ transition region is tens of a.u.

The orbitals that are used to obtain the parent-ion wave functions $|\Phi_b(\mathbf{x})\rangle$ are expanded exclusively in terms of the $G^{MC}_i(\mathbf{x}_1)$ functions. In the present atomic case, this is not a relevant issue, but, in the case of molecules, it accelerates convergence in terms of angular momenta (this is due to the multicenter character of this set of functions in the molecular case). The parent-ion wave functions are calculated by using the configuration-interaction (CI) method in the complete active space self-consistent-field (CASSCF) approach: a full CI calculation is carried out in a given active space, while simultaneously optimizing the orbitals variationally. Hence the wave functions can be written as linear combinations of either configuration state functions (CSF) or Slater determinants:

$$|\Phi_b(\mathbf{x})\rangle = \sum_i c_{ib}\left|{}^{2S_b+1}_q\,\Xi_i(\mathbf{x})\right\rangle = \sum_i c'_{ib}|D_i(\mathbf{x})\rangle, \tag{8}$$

where $|^{2S_b+1}_{q}\Xi_i(\mathbf{x})\rangle$ represents an $(N-1)$-electron CSF with multiplicity $2S_b+1$ and symmetry q, and $|D_i(\mathbf{x})\rangle$ is a Slater determinant. Going from one representation to the other is possible by means of the graphical unitary group approach (GUGA) [69]. We use both the CSFs to have well defined total spin and symmetry and the Slater determinants in the framework of the second quantization theory to obtain the N-electron states [70]:

$$\left|\bar{\Phi}_{bi}(\mathbf{x})\right\rangle = \sum_j c'_{jb} a_i^\dagger |D_j(\mathbf{x})\rangle, \tag{9}$$

where $\bar{\Phi}_{bi}$ describes the parent ion b augmented in the orbital i. These orbitals are expressed in terms of the $\{G_i^{MC}(\mathbf{x}_1)\}$ and the $G_i^{SC}(\mathbf{x}_1)$ functions. All computations that exclusively rely on Gaussian functions, $(N-1)$-electron target states, N-electron configurations obtained through Eq. (9), operators matrix elements, etc., are obtained by using MOLPRO and MOLCAS packages [17,50]. Specifically, we use the former for the CASSCF calculation yielding the initial parent-ion wave functions and the latter for the augmentation procedure and subsequent calculation of operator matrix elements.

If the R_0 radius (i.e., the distance at which B-splines start) is chosen so that the density of the parent-ion states included in the CC expansion [Eq. (2)] is negligible beyond that point, which is not difficult to achieve because these target states are expressed in terms of the short-range $\{G_i^{MC}(\mathbf{x}_1)\}$ functions, then the permutation of an electron whose wave function is exclusively described by the B-spline functions with the rest of the $N-1$ electrons described by the $\{G_i^{MC}(\mathbf{x}_1)\}$ functions is also negligible. This fact simplifies enormously the computation of operator matrix elements when B-splines are involved, because the direct product of an antisymmetrized parent-ion state with a B-spline is already an antisymmetric state, thus facilitating its implementation (see [49] for details). Nevertheless, one has to evaluate all mixed integrals involving the B-spline and the $G_i^{SC}(\mathbf{x}_1)$ functions. Since none of the available QCPs operate directly with B-splines, the computation of the matrix elements involving these functions has been implemented.

In summary, the key ingredients of XCHEM are the following: (i) the space partition and the basis functions selection for its representation (GABS+multicenter Gaussian expansion), (ii) the disjoint support of B-splines from the parent-ion wave functions included in the CC expansion, and (iii) the interface of MOLCAS with scattering methods, which allows us to include electron correlation at the same level as that provided by *ab initio* QCPs for bound states.

B. STOCK approach

In order to test the performance of the XCHEM approach to describe Ne photoionization, we have compared our results with those of independent numerical calculations performed with the STOCK code, for a few selected cases in which we can guarantee that the same level of electron correlation has been used. Details of the STOCK code can be found in [15]. Briefly, the method relies exclusively on B-splines as a primary basis set, and instead of explicitly imposing asymptotic boundary conditions as we do [see Eq. (6)], it makes use of the exterior complex scaling (ECS) formalism [71,72], which ensures outgoing waves in the asymptotic region. For the bound states, STOCK uses the multiconfiguration Hartree-Fock method (MCHF) [65], in which the atomic wave function is expanded as a linear combination of CSF:

$$|\Psi(\mathbf{x})\rangle = \sum_i c_i \left|^{2S+1}\Xi_i(\mathbf{x})\right\rangle, \tag{10}$$

where the set of coefficients $\{c_i\}$ and radial functions $\{R_{nl}(r)\}$ used to expand the spin orbitals are obtained from the optimization of the energy functional using the nonrelativistic atomic Hamiltonian H:

$$E[\{c_i\},\{R_{nl}(r)\}] = \langle\Psi(\mathbf{x})|H|\Psi(\mathbf{x})\rangle. \tag{11}$$

The MCHF problem is solved using the ATSP2K package [73].

We notice that the STOCK code has been especially designed to describe atomic systems, so that it is computationally more efficient than the XCHEM code to describe Ne photoionization (XCHEM has been optimized to describe molecular systems and incorporates the most common molecular point symmetries, but not the spherical one). Essentially, STOCK computes the complete scattering wave function making use of the CC expansion in Eq. (2), but at variance with the XCHEM code, it does not allow one to select a particular collection of parent-ion eigenstates $\{|\Phi_b(\mathbf{x})\rangle\}$, but all the states that diagonalize the $(N-1)$-electron Hamiltonian. Therefore, for a computation that includes electronic excitations of the target, the only way to have an equivalent CC expansion with XCHEM is to include all parent-ion eigenstates, which is extremely expensive if we are only interested in describing ionization above the lowest ionization thresholds and obtaining a good description of electron correlation. Thus we have restricted the benchmarking with the STOCK code to the case in which the parent-ion states in the CC expansion are described by the reference configuration (i.e., no further electronic excitations are allowed to optimize the parent-ion wave functions).

III. RESULTS

A. Computational details

In our CC expansion, we have included two parent ions corresponding to the configurations $1s^2 2s^2 2p^5$ ($^2P^o$) and $1s^2 2s^1 2p^6$ ($^2S^e$), which after augmentation with the $G_i^{SC}(\mathbf{x}_1)$ and B-spline bases leads to CI vectors of about one million components (each component corresponds to a different configuration) for the neutral system, for the case of maximum correlation (see below). The wave functions representing the two parent ions were computed by using different levels of correlation, depending on how the nine electrons were distributed in the space defined by the atomic orbitals. In order to create a common set of orbitals, valid for both parent ions, a state average CASSCF calculation was performed, optimizing with respect to the energetic average of the $^2S^e$ and the (triply degenerate) $^2P^o$ states. We will show results for two levels of correlation: (i) minimal CI (MCI), in which the parent-ion states are obtained using a CAS(7,4) calculation, that is, including all configurations (subject to spin and symmetry restrictions) obtained by seven electrons distributed over the $2s$, $2p_x$, $2p_y$, and $2p_z$ orbitals with the $1s$ orbital being doubly occupied always (note that this allows for comparison with the STOCK code), and (ii) extended CI (XCI), in which the active

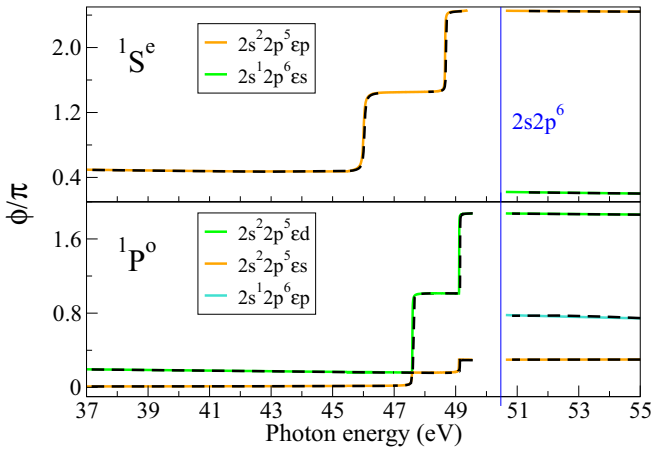

FIG. 1. Eigenphases in units of π for the scattering channels of symmetry $^1S^e$ (top panel) and $^1P^o$ (botttom panel), computed using XCHEM (dashed lines) and STOCK (solid lines) at MCI level. The region shown below the $2s2p^6$ ionization threshold (vertical line) extends from well below the resonances up to the second resonance for the two resonance series $2s2p^6ns$ and $2s2p^6np$.

space is extended from the MCI case, to allow also occupation of $3p$, $3d$, and $4s$ orbitals [i.e., a CAS(7,13) calculation].

At both MCI and XCI level, the parent ions are obtained using as localized Gaussians those defined in the standard cc-pVQZ basis set [74,75]. The virtual orbitals thus resulting from the calculation at either level of theory are disregarded in the augmentation procedure; i.e., the extra electron may only be found either in orbitals contained in the active space of the parent ions or in orbitals created by the addition of the GABS basis. Failure to do so would result in the inclusion of highly diffuse localized orbitals. These may protrude into the B-spline part of the GABS basis, and would thus render moot the assumption of zero overlap between localized Gaussians and B-splines.

The GABS basis consists of B-splines of order $k = 7$ starting at $R_0 = 7$ a.u. with a node separation of 0.5 a.u. in a box of 200 a.u., and a set of Gaussian functions $[G_{iK}^{\ell m}(\vec{r}) = N_{i\ell} r^{K_\ell} e^{-\alpha_i r^2} X_{\ell m}(\hat{r})]$ with an even-tempered sequence of α_i exponents as that used in [49] and $K_\ell = \ell + 2k$ values with $\ell_{\max} = 3$ and $k_{\max} = 2$. For the parent ions we have considered, we only need a photoelectron angular momentum up to $\ell = 2$ to describe the $^1S^e$ and $^1P^o$ total symmetries. This choice leads to the following powers of r according to the angular momentum: $K_0 = 0,2,4$, $K_1 = 1,3,5$, and $K_2 = 2,4,6$.

B. Photoionization of Ne at MCI level

At this level of correlation we can compare, on an equal footing, the XCHEM results with those obtained with STOCK, as explained in Sec. II B. Figure 1 shows the eigenphases computed for the scattering channels with $^1S^e$ and $^1P^o$ symmetries using both approaches at the MCI level. For the former symmetry, which is the same as for the ground state, the continuum above the lowest ionization threshold corresponds to a state in which the $2s^22p^5$ parent ion is coupled with an outer electron described by a p wave: $2s^22p^5\epsilon p$. Above the $2s2p^6$ threshold, a new continuum emerges for the same symmetry: $2s2p^6\epsilon s$. For the $^1P^o$ symmetry, we have multiple channels both below and above the $2s2p^6$ threshold: $2s^22p^5\epsilon s$ and $2s^22p^5\epsilon d$ below the $2s2p^6$ threshold and the additional channel $2s2p^6\epsilon p$ above. Below the $2s2p^6$ threshold, the continuum contains a single resonance series: $2s2p^6ns$ and $2s2p^6np$ for the $^1S^e$ and $^1P^o$ symmetries, respectively. The agreement between the XCHEM and STOCK eigenphases is excellent, both in the resonant and nonresonant regions.

Notice the pronounced jumps in the phases when one goes through the resonances. The total phase shift, built up from the sum over all the eigenphases $\phi(E) = \sum \phi_\mu(E)$, experiences a variation of π when going from well below to well above the resonance and fulfills the analytical form [76]:

$$\phi(E) = \phi^0(E) + \arctan\left(\frac{\Gamma}{2(E_r - E)}\right), \tag{12}$$

where E_r is the resonance energy and $\phi^0(E)$ is the background of the total phase. From the fit of the computed total phase to Eq. (12), the resonance energy and width can be determined. The individual eigenphases fulfill the equation [77]

$$2(E - E_r) = \sum_{\mu=1}^{N} \Gamma_\mu \cot\left(\phi_\mu^0 - \phi_\mu(E)\right), \tag{13}$$

where $\phi_\mu(E)$ and ϕ_μ^0 stand for the eigenphase and its corresponding background, respectively, and $\nu = 1,2,\ldots,N$, N being the number of open channels for the chosen symmetry. The partial autoionization width, Γ_μ, measures the strength of the interaction between the resonance and the scattering channel μ, and its sum over all the open channels gives the total width $\Gamma = \sum \Gamma_\mu$. Hence the ratio Γ_μ/Γ, usually known as branching ratio, gives the probability the resonance has to decay into the different open channels, which is relevant information to understand the decay dynamics of these short-lived states. From Eq. (13), we obtain for the two open channels of $^1P^o$ symmetry

$$\frac{\Gamma_1}{\Gamma_2} = -\frac{\tan\left(\phi_\nu(E_r) - \phi_1^0\right)}{\tan\left(\phi_\nu(E_r) - \phi_2^0\right)}, \quad \nu = 1,2. \tag{14}$$

Equation (14) can be used to compute the Γ_1/Γ_2 ratio. Notice that, in contrast with the total phase, the partial eigenphases experience a variation smaller than π radians in the vicinity of the resonances. Figure 1 shows, however, that in the vicinity of the $2s2p^6np$ resonances, the $2s^22p^5\epsilon d$ eigenphase takes most of the π jump. This indicates that the decay of these resonances to the $2s^22p^5\epsilon d$ continuum is the dominant process, as expected by propensity rules [78].

The $2s2p^6np$ resonant series also leaves its fingerprint in the photoionization cross section in the form of Fano-like peaks, due to the interference between the direct and resonance mediated ionization paths [56]. The partial photoionization cross section corresponding to a channel μ is given by

$$\sigma_\mu^L = \frac{4\pi^2(E - E_g)}{c} |\langle \Psi_{\mu E}^- | \hat{\epsilon} \cdot \sum \vec{r}_i | \Psi_g \rangle|^2,$$
$$\sigma_\mu^V = \frac{4\pi^2}{c(E - E_g)} |\langle \Psi_{\mu E}^- | \hat{\epsilon} \cdot \sum \vec{p}_i | \Psi_g \rangle|^2, \tag{15}$$

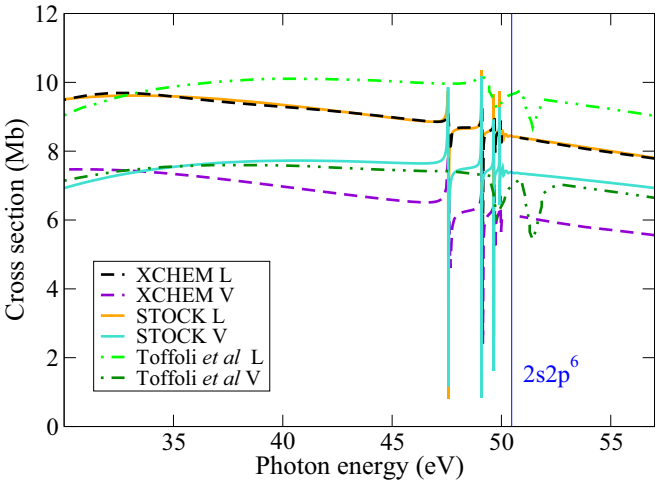

FIG. 2. Total photoionization cross section from the ground state of Ne, computed using XCHEM (dashed lines) and STOCK (solid lines) at MCI level, for lenght (L) and velocity (V) gauges. Results from Toffoli *et al.* [48], obtained by using the same level of correlation, are also shown (dashed-dotted lines). The vertical line indicates the position of the $2s2p^6$ ionization threshold.

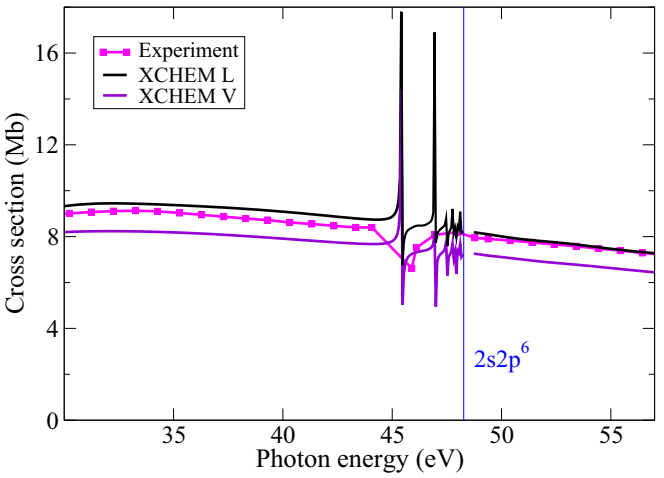

FIG. 3. Total photoionization cross section from the ground state of Ne, computed using XCHEM (solid lines) at the XCI level, for lenght (L) and velocity (V) gauges. Absolute cross sections measured by Samson *et al.* [86] are also shown (solid line with squares). The vertical line indicates the position of the $2s2p^6$ ionization threshold.

where the superscripts L and V stand for the length and velocity gauges, respectively. The polarization of the incident light is $\hat{\epsilon}$, c is the speed of light, and E_g the ground-state energy.

Figure 2 shows the total photoionization cross section ($\sigma = \sum \sigma_\mu$), computed with XCHEM and STOCK at MCI level, for length and velocity gauges. Independent theoretical results obtained by other authors, at the same level of correlation, are also shown [48]. The results of XCHEM and STOCK in length gauge are indistinguishable to the naked eye. However, in the velocity gauge, the slopes of the corresponding nonresonant backgrounds are different, while the position and shape of the resonance peaks remain similar. Since both calculations were performed at MCI level, the difference in the background can only be explained by differences in the basis functions used in those calculations: a hybrid Gaussian and B-spline basis in XCHEM and a purely B-spline one in STOCK . As explained above, in XCHEM, B-spline functions are only used beyond R_0, which means that the short-range part description of the continuum wave function is entirely described by Gaussian functions. In contrast, in STOCK B-splines are used all the way from the origin to the asymptotic region. B-spline functions provide more flexibility than Gaussian functions, in particular, they can better describe the wave-function cusp at $r = 0$. Hence it is not surprising that discrepancies are only seen in the velocity gauge, since it emphasizes the contribution of the short-range part of the wave function. This is possibly the reason why, in the velocity gauge, the nonresonant background of Ref. [48] (an all-B-spline calculation) is in better agreement with STOCK than with XCHEM . Nevertheless, the resonant peaks predicted in [48] are shifted around 2.2 eV to higher energies, thus suggesting a poorer representation of electron correlation in the resonant states.

C. Photoionization of Ne at XCI level

Figure 3 shows the total cross sections again, but this time computed at the XCI level with XCHEM . They are compared with the experimental values reported in [86]. The comparison is made on absolute scale (no rescaling of either the calculated or the measured cross sections). As can be seen, the agreement between theory and experiment is very good. Also, the results obtained in the length and velocity gauges are much closer to each other than in Fig. 2, which is the natural consequence of having used a much larger configuration expansion. Another difference with Fig. 2 is that the resonant peaks are displaced to lower energies, thus indicating an even better description of electron correlation in the resonant states. Interestingly, the XCHEM result computed in length gauge is closer to the measured data than that obtained in velocity gauge. This fact stresses once again that the quality of the wave functions in the short-range domain, though acceptable, is not as good as in the middle and long ranges, due to the intrinsic limitations of the Gaussian expansion in the innermost region.

Let us now analyze in more detail the resonance structures observed in the spectrum. We have evaluated the resonance parameters by fitting the calculated total cross section to the formula [57]:

$$\sigma(E) = \sigma^0(E)\left[\rho^2\frac{(q+\epsilon)^2}{\epsilon^2+1} + 1 - \rho^2\right], \qquad (16)$$

where $\sigma^0(E)$ is the total cross section background (a smooth function of the energy), $\epsilon = \frac{2(E-E_r)}{\Gamma}$ is the reduced energy, q the Fano parameter, and ρ^2 the correlation parameter ($0 \leqslant \rho^2 \leqslant 1$). This formula is a generalization of the usual Fano formula to the case of multichannel photoionization. Notice that the usual single-channel Fano formula is recovered when $\rho^2 = 1$, so that ρ is a measure of the correlation between the different open channels in the photoionization process.

Table I shows the results obtained from the fit of the cross sections calculated at XCI correlation level. We have extracted the energy E_r, total autoinization width Γ, profile parameter q, and correlation parameter ρ^2 for the lowest three $^1P^o$ resonances converging to the $2s2p^6$ ionization threshold. For consistency, energies and widths have also been

TABLE I. Resonance parameters for the lowest three $^1P^o$ resonances converging to the $2s2p^6$ threshold. The XCHEM results at the XCI level (highlighted in bold) have been obtained in three different ways: by fitting the total phase shift and by fitting the total cross sections obtained in length and velocity gauges. The results are compared with theoretical and experimental values reported in the literature. Uncertainties, where quoted, are given in parentheses and experimental values are given in italics for an easy identification.

Resonance	Energy (eV)	Width (meV)	Profile parameter q	Correlation coefficient ρ^2
$2s2p^63p$	**45.431**[a,b,c]	**15.0**[a,b]	**–1.47**[b]	**0.79**[b]
	45.5442(50)[d]	**15.1**[c]	**–1.34**[c]	**0.77**[c]
	45.546(8)[f]	*16(2)*[d]	*–1.58(1)*[e]	*0.75(5)*[e]
	45.53397[d]	*13(2)*[e,f]	*–1.6(2)*[f]	*0.70(7)*[f]
	45.557[e]	13[g]	–1.59(1)[e]	0.72[e]
	49.725[g]	18.6(10)[e]	–1.53(1)[e]	0.73[e]
	46.253[h]	34.9[d]	–1.4[g]	0.77[g,j]
	45.5655[i]	13.9[h]	–3.69[h]	0.514[h]
	45.538[k]	11.4[i]	–0.34[j]	0.93[j]
		11.7[j]	–1.16[j]	0.91[j]
		12.1[j]	–1.61[j]	0.76[j]
		31.8[k]	–1.30[j]	
			–1.32[k]	
$2s2p^64p$	**46.942**[a,b,c]	**4.3**[a,b,c]	**–1.26**[b]	**0.84**[b]
	47.1193(50)[d]	*5.7(10)*[e]	**–1.67**[c]	**0.85**[c]
	47.121(5)[f]	*4.5(1.5)*[f]	*–1.47(1)*[e]	*0.78(11)*[e]
	47.11092[d]	7[g]	*–1.6(3)*[f]	*0.70(7)*[f]
	47.111[e]	4.3[e]	–1.88[e]	0.72[e]
	51.318[g]	6.65[d]	–1.82[e]	0.73[e]
	47.397[h]	3.86[h]	–1.35[g]	0.63[g]
	47.1278[i]	5.28[i]	–3.95[h]	0.505[h]
		3.8[j]	–1.75[j]	0.76[j]
			–1.46[j]	0.77[j]
$2s2p^65p$	**47.506**[a]	**1.6**[a]	**–1.35**[b]	**0.86**[b,c]
	47.502[b,c]	**1.7**[b,c]	**–1.78**[c]	*0.6(2)*[e]
	47.6952(15)[d]	*3.6(18)*[e]	*–1.46(5)*[e]	*0.70(14)*[f]
	47.692(5)[f]	*2(1)*[f]	*–1.6(5)*[f]	0.74[e]
	51.894[g]	2.47[d]	–1.9[e]	0.75[e]
	47.687[e]	1.8[e]	–1.87[e]	0.71[g]
	47.69182[d]	3[g]	–1.15[g]	0.502[h]
	47.814[h]	1.62[h]	–4.05[f]	
	47.6975[i]	2.61[i]		

[a]XCHEM: fit of the total phase.
[b]XCHEM: fit of the total cross section in length gauge.
[c]XCHEM: fit of the total cross section in velocity gauge.
[d]Reference [79].
[e]Reference [80].
[f]Reference [55].
[g]Reference [81].
[h]Reference [82].
[i]Reference [83].
[j]Reference [84].
[k]Reference [85].

evaluated by fitting the total scattering phases to Eq. (12). All parameters have been evaluated by using results obtained in both length and velocity gauge, and are compared with previously reported theoretical and experimental results (we do not compare the values of the total cross-section background because all measurements but those of [86]—see Fig. 3—were reported in arbitrary units). It is worth noticing that among the four resonance parameters, q is the most sensitive one to the quality of the basis, because it depends both on the coupling between the discrete state embedded in the continuum and the nonresonant continuum components, and on the dipole coupling between the ground and the modified discrete state (perturbed discrete state due to the nonzero coupling with the nonresonant continuum). As can be seen, values of the resonance energies are very close for the different computation schemes (in percent), while ρ^2, Γ, and q exhibit a higher dispersion. It is worth noticing that the other theoretical results shown in the table were obtained by using very different levels of theory: the relativistic random-phase approximation (RRPA) together with

the relativistic multichannel quantum-defect theory (RMQDT) [81], the R-matrix method, sometimes combined with the multichannel quantum-defect theory (MQDT) [79,80,83,84], the time-dependent local-density approximation (TDLDA) [82], and the time-dependent configuration-interaction singles (TDCIS) [85].

Considering the XCHEM results only, the E_r, Γ, and ρ^2 parameters obtained from the different fits agree very well with each other. For the Fano q parameter, differences between the results extracted from the length and the velocity gauges are larger. The XCHEM resonance energies are 0.1–0.2 eV lower than the experimental ones, and are comparable or even better than those obtained from other theoretical methods. The agreement with the experimental total widths is also quite good: the computed values are within the experimental error bars or pretty close. For the q parameters, apart from the slight gauge discrepancy indicated above, the agreement with the experimental values is quite acceptable.

From the partial cross sections, one can get information about the decay of the resonances to the different open channels. As shown by Starace [63], the photoionization partial cross sections can be written as

$$\sigma_\mu(\epsilon) = \frac{\sigma_\mu^0(\epsilon)}{\epsilon^2+1}\{\epsilon^2 + 2\epsilon[q\,\mathrm{Re}(\alpha_\mu) - \mathrm{Im}(\alpha_\mu)] + 1 - 2q\,\mathrm{Im}(\alpha_\mu) - 2\,\mathrm{Re}(\alpha_\mu) + (q^2+1)|\alpha_\mu|^2\}, \quad (17)$$

where $\sigma_\mu^0(\epsilon)$ is the partial cross-section background and $\alpha_\mu = \mathrm{Re}(\alpha_\mu) + i\,\mathrm{Im}(\alpha_\mu)$ is the Starace parameter [63]. The α_μ parameters are not independent of each other; they fulfill the following relation:

$$\sum_\mu \sigma_\mu^0(\epsilon)|\alpha_\mu|^2 = \sigma^0(\epsilon)\rho^2, \quad (18)$$

where $\sigma^0(\epsilon)$ and ρ^2 are the background and the correlation parameters, respectively, appearing in the total cross section. Figure 4 shows the $2p^{-1}\epsilon s$ and $2p^{-1}\epsilon d$ partial cross sections around the $2s2p^63p$, $2s2p^64p$, and $2s2p^65p$ resonances. As expected, the $2p^{-1}\epsilon d$ channel clearly dominates the photoionization process. Only when the partial cross section associated with the dominant channel undergoes a very pronounced dip in the vicinity of the resonances, the $2p^{-1}\epsilon s$ partial cross section takes over, but only in very narrow energy intervals.

It is easy to demonstrate that

$$\frac{\Gamma_\nu}{\Gamma_\mu} = \frac{\sigma_\nu^0|\alpha_\nu|^2}{\sigma_\mu^0|\alpha_\mu|^2}, \quad (19)$$

so, in principle, if we were able to extract the backgrounds σ_μ^0 and the Starace parameters α_μ by fitting the partial cross sections to Eq. (17), then we could get the branching ratios from (19). The problem lies now on how to perform the fitting. The partial cross sections, like the total one, are nonlinear functions of the fitting parameters, but extracting the resonance parameters from the partial ones has two additional complications: (i) there are extra parameters, namely the α_μ, and (ii) the α_μ parameters belonging to different channels are not independent [as shown by Eq. (18)]. For this reason, for each partial cross section, we will fix the parameters already obtained from the fit of the total cross section (E_r, Γ, and q) and will only leave three free parameters: $\mathrm{Re}(\alpha_\mu)$, $\mathrm{Im}(\alpha_\mu)$, and σ_μ^0. The parameters must be determined by imposing simultaneously the condition given by Eq. (18). Due to this additional condition, for many initial values of the α_μ parameters convergence is not reached or leads to absurd values. To double check the results of this fitting procedure, we have also adopted the following procedure. We have linearized Eq. (17), by introducing the new parameters $C_{1\mu}$ and $C_{2\mu}$ [87] defined as

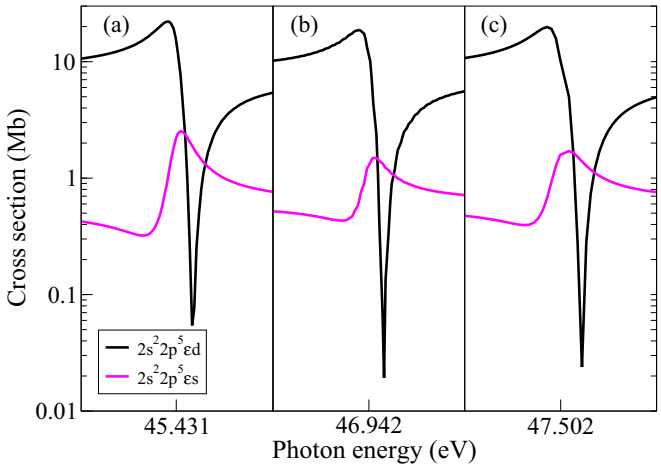

FIG. 4. Partial photoionization cross sections computed using XCHEM at the XCI level and in velocity gauge. The three panels (a), (b), and (c) display the energy region ($[E_r - 4\Gamma, E_r + 4\Gamma]$) around the $2s2p^63p$ ($\Gamma = 15.1$ meV), $2s2p^64p$ ($\Gamma = 4.3$ meV), and $2s2p^65p$ ($\Gamma = 1.7$ meV) resonances, respectively, which can decay into the $2s^22p^5\epsilon s$ and the $2s^22p^5\epsilon d$ continua.

$$C_{1\mu} = 2[q\,\mathrm{Re}(\alpha_\mu) - \mathrm{Im}(\alpha_\mu)],$$
$$C_{2\mu} = 1 - 2q\,\mathrm{Im}\alpha_\mu - 2\,\mathrm{Re}(\alpha_\mu) + (q^2+1)|\alpha_\mu|^2, \quad (20)$$

so that Eq. (17) results in

$$\sigma_\mu(\epsilon) = \frac{\sigma_\mu^0(\epsilon)}{\epsilon^2+1}(\epsilon^2 + C_{1\mu}\epsilon + C_{2\mu}). \quad (21)$$

This way, only the positions and widths of the resonances are fixed. There is one last and important thing to be taken into account, which is the boundary conditions for $C_{1\mu}$ and $C_{2\mu}$. From Eq. (20), the α_μ parameters are determined from a quadratic equation, so that two roots are obtained:

$$\mathrm{Re}(\alpha_\mu) = \frac{qC_{1\mu} + 2 \pm \sqrt{4C_{2\mu} - C_{1\mu}^2}}{2(1+q^2)},$$
$$\mathrm{Im}(\alpha_\mu) = \frac{q\left(2 \pm \sqrt{4C_{2\mu} - C_{1\mu}^2}\right) - C_{1\mu}}{2(1+q^2)}. \quad (22)$$

From the fact that $\mathrm{Re}(\alpha_\mu)$ and $\mathrm{Im}(\alpha_\mu)$ must be real numbers, one obtains $4C_{2\mu} \geqslant C_{1\mu}^2$. This condition must be imposed during the fitting process in order to get meaningful results, because it reflects the fact that the partial cross section is a non-negative quantity. This constraint in $C_{1\mu}$ and $C_{2\mu}$ also manifests in the universal scaling of the resonances, as described, e.g., in Refs. [88,89]. Then one has to select the correct Starace parameter from the two solutions of Eq. (22). For this we can use Eq. (18) to find the roots that better fulfill this condition. Actually most of the roots rejected following

TABLE II. Starace parameters and branching ratios (Γ_μ/Γ) for the same resonances as in Table I. The coefficients $C_{1\mu}$ and $C_{2\mu}$ and its error bars (in brackets), obtained through the fitting to the partial cross sections using (21), are also shown.

Resonance	μ	$C_{1\mu}$	$C_{2\mu}$	Re(α_μ)	Im(α_μ)	Γ_μ/Γ
$2s2p^63p$	$2s^22p^5\epsilon s$	2.451(0.009)[a]	4.151(0.014)[a]	−0.770[a]	−0.097[a]	0.046[c]
		1.971(0.008)[b]	3.443(0.010)[b]	−0.677[b]	−0.079[b]	0.044[d]
						0.049[e]
	$2s^22p^5\epsilon d$	−2.649(0.008)[a]	1.754(0.012)[a]	0.934[a]	−0.045[a]	0.954[c]
		−2.391(0.008)[b]	1.429 (0.011)[b]	0.931[b]	−0.051[b]	0.956[d]
						0.951[e]
$2s2p^64p$	$2s^22p^5\epsilon s$	1.352(0.009)[a]	2.200(0.010)[a]	−0.453[a]	−0.105[a]	0.022[c]
		1.663(0.007)[b]	2.246(0.009)[b]	−0.432[b]	−0.111[b]	0.021[d]
						0.021[e]
	$2s^22p^5\epsilon d$	−2.301(0.011)[a]	1.392(0.017)[a]	0.846[a]	0.085[a]	0.978[c]
		−3.145(0.013)[b]	2.600(0.024)[b]	0.863[b]	0.132[b]	0.979[d]
						0.979[e]
$2s2p^65p$	$2s^22p^5\epsilon s$	1.798(0.041)[a]	2.493(0.052)[a]	−0.536[a]	−0.176[a]	0.025[c]
		2.167(0.038)[b]	2.581(0.053)[b]	−0.507[b]	−0.180[b]	0.025[d]
						0.024[e]
	$2s^22p^5\epsilon d$	−2.544(0.027)[a]	1.618(0.042)[a]	0.963[a]	−0.028[a]	0.975[c]
		−3.395(0.024)[b]	2.882(0.046)[b]	0.964[b]	−0.018[b]	0.975[d]
						0.976[e]

[a]Fit of the partial cross section in length gauge.
[b]Fit of the partial cross section in velocity gauge.
[c]Using Eq. (19) in length gauge.
[d]Using Eq. (19) in velocity gauge.
[e]Using Eq. (14).

this selection criteria imply a correlation parameter $\rho^2 > 1$, which is outside its validity range. Nevertheless, if there are more than two roots that satisfy reasonably well Eq. (18), then we cannot be certain about which one is correct and we need extra information to remove the ambiguity, for instance, by computing the branching ratios using an independent method.

The results obtained for $C_{1\mu}$, $C_{2\mu}$, α_μ, and Γ_μ/Γ using the different methods are shown in Table II. The gauge invariance of the Starace parameters is worse than that of partial widths Γ_μ but better than that of the q parameter. The values of the partial widths obtained with different methods agree very well with each other. These numbers confirm the known qualitative behavior: 95% of the decay of the first resonance goes into the $2p^{-1}\epsilon d$ channel, and 98% of the second and the third resonances.

The interference between the two open scattering channels $2p^{-1}\epsilon s$ and $2p^{-1}\epsilon d$ below the $2s2p^6$ ionization threshold manifests in the electron angular distribution, which, for incident linearly polarized light, is given in terms of the β asymmetry parameter [90,91]:

$$\frac{d\sigma(E)}{d\hat{k}} = \frac{\sigma(E)}{4\pi}[1 + \beta P_2(\cos\theta)], \tag{23}$$

where P_2 is the second-order Legendre polynomial and θ is the electron emission angle referred to the polarization direction. In Fig. 5 we compare the results obtained with XCHEM near the $2s2p^63p$, $2s2p^64p$, and $2s2p^65p$ resonances with the experimental ones reported in Ref. [80]. For completeness we also compare with Ref. [80] the total photoionization cross section near the same resonances. For a better visualization, our results have been shifted by 0.126, 0.170, and 0.185 eV for the first, the second, and the third resonance, respectively. These energy shifts correspond to the differences between the resonance positions reported in Ref. [80] and the XCHEM ones given in Table I. As expected from the results reported in this

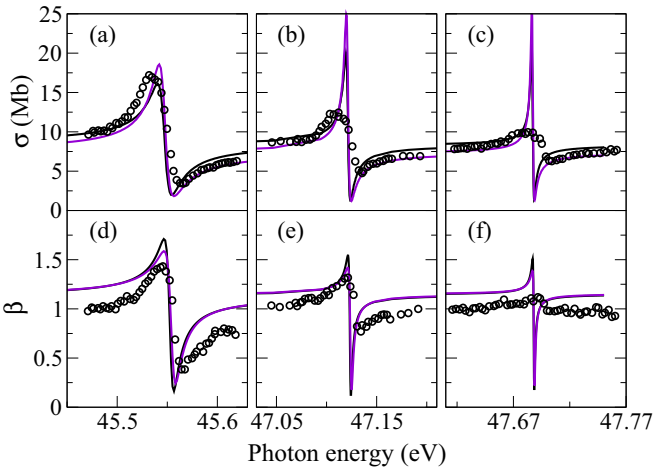

FIG. 5. Total photoionization cross sections [panels (a), (b), and (c)] and β asymmetry parameter [panels (d), (e), and (f)] near the $2s2p^63p$, $2s2p^64p$, and $2s2p^65p$ resonances. Solid lines: our results in length (black) and velocity (purple) gauges; black circles: experimental results digitized from Ref. [80]. As explained in the text, the theoretical results have been shifted in energy by 0.126, 0.170, and 0.185 eV for the first, the second, and the third resonance, respectively.

table, the agreement for the total photoionization cross sections is quite good. For the β parameter, which is much more sensitive to the level of correlation included in the calculation, the discrepancy with experiment is higher, around 15%–20% in the nonresonant region, although the resonant profiles are reasonably reproduced. These discrepancies are comparable to those reported in [80] when comparing with results obtained by using the R-matrix method.

IV. CONCLUSION

We have used the XCHEM approach to study multichannel photoionization of Ne in the vicinity of the autoionizing states lying between the $2s^2 2p^5$ and $2s2p^6$ ionization thresholds. This is the first application of the XCHEM approach to the case in which the remaining cation is a multielectron target. Comparison with the results of independent benchmark calculations with the STOCK code, performed at the same level of theory, demonstrates the good performance of our approach. Our calculated total photoionization cross sections, obtained at the XCI level, are also in very good agreement with the absolute ones measured by Samson *et al.* [86]. From these results, we have extracted resonance parameters, namely, resonance positions, total autoionization widths, Fano profile parameters, and correlation parameters for the lowest three autoionizing states. These are in good agreement with those reported in earlier theoretical and experimental work.

We have gone a step further and evaluated β asymmetry parameters and partial photoionization cross sections and, from them, partial autoionization widths and Starace parameters for the lowest three resonances. Our results confirm earlier expectations that the resonances of $^1P^o$ symmetry converging to the $2s2p^6$ threshold are much more likely to decay into the $2p^{-1}\epsilon d$ continuum than into the $2p^{-1}\epsilon s$ one [85], but we have now quantified how much likely: 95% vs 5%, respectively, for the lowest resonance, and 98% and 2% for the other two resonances. We have also shown that, in very narrow ranges of the photoelectron energy, in the vicinity of the resonances, the partial $2p^{-1}\epsilon s$ cross section can be larger than the $2p^{-1}\epsilon d$ one, in contrast with the expectation that the latter should amply dominate in the whole energy range.

These results show the capabilities of the XCHEM code to describe electron correlation in the continuum and hence autoionization decay in multielectron systems, which is of crucial importance in the case of molecular targets and for which the XCHEM code has been designed. In fact, the description of atomic systems with the XCHEM code is more challenging than that of molecular systems, since one cannot use multicenter Gaussian expansions without compromising spherical symmetry. In particular, it is hard to preserve the degeneracy of thresholds, which implies that rather large powers of the Gaussian preexponential factors (K_ℓ) must be used to obtain an accurate representation of continuum states in the short and middle ranges. This gives us confidence that the description of resonant molecular photoionization with the XCHEM code should be rather straightforward.

ACKNOWLEDGMENTS

We acknowledge computer time from the CCC-UAM and Marenostrum Supercomputer Centers, and financial support from the European Research Council under the European Union's Seventh Framework Programme (No. FP7/2007-2013)/ERC Grant Agreement No. 290853 XCHEM, the MINECO Projects No. FIS2013-42002-R and No. FIS2016-77889-R, and the European COST Action XLIC CM1204 and STSM CM1204-26542. L.A. acknowledges support from the TAMOP NSF Grant No. 1607588, as well as UCF fundings. E.L. and T.K. acknowledge support from the Swedish Research Council, Grant No. 2016-03789.

[1] M. Schöffler, J. Titze, N. Petridis, T. Jahnke, K. Cole, L. P. H. Schmidt, A. Czasch, D. Akoury, O. Jagutzki, J. B. Williams *et al.*, Science **320**, 920 (2008).

[2] T. Jahnke, H. Sann, T. Havermeier, K. Kreidi, C. Stuck, M. Meckel, M. Schöffler, N. Neumann, R. Wallauer, S. Voss *et al.*, Nat. Phys. **6**, 139 (2010).

[3] M. Dell'Angela, T. Anniyev, M. Beye, R. Coffee, A. Föhlisch, J. Gladh, T. Katayama, S. Kaya, O. Krupin, J. LaRue *et al.*, Science **339**, 1302 (2013).

[4] F. Calegari, D. Ayuso, A. Trabattoni, L. Belshaw, S. De Camillis, S. Anumula, F. Frassetto, L. Poletto, A. Palacios, P. Decleva *et al.*, Science **346**, 336 (2014).

[5] C. Ott, A. Kaldun, L. Argenti, P. Raith, K. Meyer, M. Laux, Y. Zhang, A. Blättermann, S. Hagstotz, T. Ding *et al.*, Nature (London) **516**, 374 (2014).

[6] E. P. Månsson, D. Guénot, C. L. Arnold, D. Kroon, S. Kasper, J. M. Dahlström, E. Lindroth, A. S. Kheifets, A. L'Huillier, S. L. Sorensen *et al.*, Nat. Phys. **10**, 207 (2014).

[7] P. M. Kraus, B. Mignolet, D. Baykusheva, A. Rupenyan, L. Horný, E. F. Penka, G. Grassi, O. I. Tolstikhin, J. Schneider, F. Jensen *et al.*, Science **350**, 790 (2015).

[8] V. Gruson, L. Barreau, Á. Jiménez-Galan, F. Risoud, J. Caillat, A. Maquet, B. Carré, F. Lepetit, J.-F. Hergott, T. Ruchon *et al.*, Science **354**, 734 (2016).

[9] M. Nisoli, P. Decleva, F. Calegari, A. Palacios, and F. Martín, Chem. Rev. (2017), doi: 10.1021/acs.chemrev.6b00453.

[10] B. W. J. McNeil and N. R. Thompson, Nat. Photon. **4**, 814 (2010).

[11] P. G. Burke, *R-Matrix Theory of Atomic Collisions*, Springer Series on Atomic, Optical, and Plasma Physics Vol. 61 (Springer, Berlin, Heidelberg, 2011).

[12] J. Tennyson, Phys. Rep. **491**, 29 (2010).

[13] O. Zatsarinny and K. Bartschat, J. Phys. B **46**, 112001 (2013).

[14] L. Argenti, R. Pazourek, J. Feist, S. Nagele, M. Liertzer, E. Persson, J. Burgdörfer, and E. Lindroth, Phys. Rev. A **87**, 053405 (2013).

[15] T. Carette, J. M. Dahlström, L. Argenti, and E. Lindroth, Phys. Rev. A **87**, 023420 (2013).

[16] F. Aquilante, J. Autschbach, R. K. Carlson, L. F. Chibotaru, M. G. Delcey, L. De Vico, I. Fdez. Galván, N. Ferré, L. M. Frutos, L. Gagliardi *et al.*, J. Comput. Chem. **37**, 506 (2016).

[17] H.-J. Werner, P. J. Knowles, G. Knizia, F. R. Manby, and M. Schütz, WIREs Comput. Mol. Sci. **2**, 242 (2012).

[18] H. Lischka, R. Shepard, R. M. Pitzer, I. Shavitt, M. Dallos, T. Muller, P. G. Szalay, M. Seth, G. S. Kedziora, S. Yabushita *et al.*, Phys. Chem. Chem. Phys. **3**, 664 (2001).

[19] H. Lischka, T. Müller, P. G. Szalay, I. Shavitt, R. M. Pitzer, and R. Shepard, WIREs Comput. Mol. Sci. **1**, 191 (2011).

[20] K. Aidas, C. Angeli, K. L. Bak, V. Bakken, R. Bast, L. Boman, O. Christiansen, R. Cimiraglia, S. Coriani, P. Dahle *et al.*, WIREs Comput. Mol. Sci. **4**, 269 (2014).

[21] M. W. Schmidt, K. K. Baldridge, J. A. Boatz, S. T. Elbert, M. S. Gordon, J. H. Jensen, S. K. N. Matsunaga, K. Nguyen, S. Su, T. L. Windus *et al.*, J. Comput. Chem. **14**, 1347 (1993).

[22] M. J. Frisch, G. W. Trucks, H. B. Schlegel, G. E. Scuseria, M. A. Robb, J. R. Cheeseman, G. Scalmani, V. Barone, B. Mennucci, G. A. Petersson *et al.*, *Gaussian 09 Revision D.01* (Gaussian Inc., Wallingford, England, 2009).

[23] H. Jørgen, A. Jensen, P. Jørgensen, and H. Ågren, J. Chem. Phys. **87**, 451 (1987).

[24] A. T. B. Gilbert, N. A. Besley, and P. M. W. Gill, J. Phys. Chem. A **112**, 13164 (2008).

[25] A. B. Rocha, J. Chem. Phys. **134**, 024107 (2011).

[26] I. Corral, J. González-Vázquez, and F. Martín, J. Chem. Theory Comput. **13**, 1723 (2017).

[27] A. Macías, F. Martín, A. Riera, and M. Yáñez, Phys. Rev. A **36**, 4179 (1987).

[28] A. Macías, F. Martín, A. Riera, and M. Yáñez, Phys. Rev. A **36**, 4187 (1987).

[29] A. Macías, F. Martín, A. Riera, and M. Yáñez, Phys. Rev. A **36**, 4203 (1987).

[30] A. Macías, F. Martín, A. Riera, and M. Yáñez, Int. J. Quantum Chem. **33**, 279 (1988).

[31] I. Sánchez and F. Martín, J. Chem. Phys. **106**, 7720 (1997).

[32] I. Sánchez and F. Martín, J. Phys. B **30**, 679 (1997).

[33] F. Martín, J. Phys. B **32**, R197 (1999).

[34] Y. V. Vanne, A. Saenz, A. Dalgarno, R. C. Forrey, P. Froelich, and S. Jonsell, Phys. Rev. A **73**, 062706 (2006).

[35] W. Vanroose, D. A. Horner, F. Martín, T. N. Rescigno, and C. W. McCurdy, Phys. Rev. A **74**, 052702 (2006).

[36] L. Tao, C. W. McCurdy, and T. N. Rescigno, Phys. Rev. A **82**, 023423 (2010).

[37] C. de Boor, *A Practical Guide to Splines*, Applied Mathematical Sciences Vol. 27 (Springer-Verlag, New York, 2001).

[38] H. Bachau, E. Cormier, P. Decleva, J. E. Hansen, and F. Martín, Rep. Prog. Phys. **64**, 1815 (2001).

[39] T. N. Rescigno and C. W. McCurdy, Phys. Rev. A **62**, 032706 (2000).

[40] V. P. Majety and A. Scrinzi, Phys. Rev. Lett. **115**, 103002 (2015).

[41] V. P. Majety and A. Scrinzi, Photonics **2**, 93 (2015).

[42] T. N. Rescigno, D. A. Horner, F. L. Yip, and C. W. McCurdy, Phys. Rev. A **72**, 052709 (2005).

[43] F. L. Yip, C. W. McCurdy, and T. N. Rescigno, Phys. Rev. A **78**, 023405 (2008).

[44] F. L. Yip, C. W. McCurdy, and T. N. Rescigno, Phys. Rev. A **81**, 053407 (2010).

[45] F. L. Yip, C. W. McCurdy, and T. N. Rescigno, Phys. Rev. A **81**, 063419 (2010).

[46] F. L. Yip, C. W. McCurdy, and T. N. Rescigno, Phys. Rev. A **90**, 063421 (2014).

[47] T.-T. Nguyen-Dang, É. Couture-Bienvenue, J. Viau-Trudel, and A. Sainjon, J. Chem. Phys. **141**, 244116 (2014).

[48] D. Toffoli and P. Decleva, J. Chem. Theory Comput. **12**, 4996 (2016).

[49] C. Marante, M. Klinker, I. Corral, J. González-Vázquez, L. Argenti, and F. Martín, J. Chem. Theory Comput. **13**, 499 (2017).

[50] B. O. Roos, G. Karlström, P. Å. Malmqvist, and A. J. Sadlej, in *Modern Techniques in Computational Chemistry: MOTECC-91*, edited by E. Clementi (ESCOM Science Publishers B.V., New York, 1991).

[51] C. Marante, L. Argenti, and F. Martín, Phys. Rev. A **90**, 012506 (2014).

[52] R. P. Madden and K. Codling, Phys. Rev. Lett. **10**, 516 (1963).

[53] R. P. Madden and K. Codling, J. Opt. Soc. Am. **54**, 268 (1964).

[54] R. P. Madden and K. Codling, Astrophys. J. **141**, 364 (1965).

[55] K. Codling, R. P. Madden, and D. L. Ederer, Phys. Rev. **155**, 26 (1967).

[56] U. Fano, Phys. Rev. **124**, 1866 (1961).

[57] U. Fano and J. W. Cooper, Phys. Rev. **137**, A1364 (1965).

[58] O. Hassouneh, A. C. Brown, and H. W. van der Hart, Phys. Rev. A **89**, 033409 (2014).

[59] A. C. Brown and H. W. van der Hart, Phys. Rev. Lett. **117**, 093201 (2016).

[60] N. Douguet, E. V. Gryzlova, E. I. Staroselskaya, K. Bartschat, and A. N. Grum-Grzhimailo, Eur. Phys. J. D **71**, 105 (2017).

[61] N. Douguet, A. N. Grum-Grzhimailo, and K. Bartschat, Phys. Rev. A **95**, 013407 (2017).

[62] D. You, H. Fukuzawa, Y. Sakakibara, T. Takanashi, Y. Ito, G. G. Maliyar, K. Motomura, K. Nagaya, T. Nishiyama, K. Asa *et al.*, Nat. Commun. **8**, 14277 (2017).

[63] A. F. Starace, *Atomic Photoionization*, Fundamental Processes in Energetic Atomic Collisions (Springer US, Boston, MA, 1983), pp. 69–110.

[64] I. Lindgren and J. Morrison, *Atomic Many-Body Theory*, 2nd ed., Springer Series in Chemical Physics Vol. 13 (Springer-Verlag, Berlin, Heidelberg, 1982).

[65] C. F. Fischer, T. Brage, and P. Jönsson, *Computational Atomic Structure: An MCHF Approach*, 1st ed. (IOP Publishing Ltd, Bristol, UK, 1997).

[66] W. R. Johnson, *Atomic Structure Theory*, 1st ed. (Springer-Verlag, Berlin, Heidelberg, 2007).

[67] C. D. H. Chisholm, *Group Theoretical Techniques in Quantum Chemistry* (Academic Press, New York, 1976).

[68] H. Friedrich, *Scattering Theory*, 1st ed., Lecture Notes in Physics Vol. 872 (Springer, Heidelberg, 2013).

[69] *The Unitary Group for the Evaluation of Electronic Energy Matrix Elements*, 1st ed., edited by J. Hinze, Lecture Notes in Chemistry (Springer-Verlag, Heidelberg, 1981).

[70] T. Helgaker, P. Jørgensen, and J. Olsen, *Molecular Electronic-Structure Theory*, 1st ed. (John Wiley and Sons, Ltd., Chichester, England, 2000).

[71] C. A. Nicolaides and D. R. Beck, Phys. Lett. A **65**, 11 (1978).

[72] B. Simon, Phys. Lett. A **71**, 211 (1979).

[73] C. F. Fischer, G. Tachiev, G. Gaigalas, and M. R. Godefroid, Comput. Phys. Commun. **176**, 559 (2007).

[74] D. Feller, J. Comput. Chem. **17**, 1571 (1996).

[75] K. L. Schuchardt, B. T. Didier, T. Elsethagen, L. Sun, V. Gurumoorthi, J. Chase, J. Li, and T. L. Windus, J. Chem. Inf. Model. **47**, 1045 (2007).

[76] A. U. Hazi, Phys. Rev. A **19**, 920 (1979).
[77] J. Macek, Phys. Rev. A **2**, 1101 (1970).
[78] U. Fano and J. W. Cooper, Rev. Mod. Phys. **40**, 441 (1968).
[79] K. Schulz, M. Domke, R. Püttner, A. Gutiérrez, G. Kaindl, G. Miecznik, and C. H. Greene, Phys. Rev. A **54**, 3095 (1996).
[80] B. Langer, N. Berrah, R. Wehlitz, T. W. Gorczyca, J. Bozek, and A. Farhat, J. Phys. B **30**, 593 (1997).
[81] M. Nrisimhamurty, G. Aravind, P. C. Deshmukh, and S. T. Manson, Phys. Rev. A **91**, 013404 (2015).
[82] M. Stener, P. Decleva, and A. Lisini, J. Phys. B **28**, 4973 (1995).
[83] L. Liang, Y. C. Wang, and Z. Chao, Phys. Lett. A **360**, 599 (2007).
[84] P. G. Burke and K. T. Taylor, J. Phys. B **8**, 2620 (1975).
[85] E. Heinrich-Josties, S. Pabst, and R. Santra, Phys. Rev. A **89**, 043415 (2014).
[86] J. Samson and W. Stolte, J. Electron Spectrosc. Relat. Phenom. **123**, 265 (2002).
[87] L. Journel, B. Rouvellou, D. Cubaynes, J. M. Bizau, F. J. Wuilleumier, M. Richter, P. Sladeczek, K.-H. Selbmann, P. Zimmermann, and H. Bergeron, J. Phys. IV France **03**, C6-217 (1993).
[88] A. N. Grum-Grzhimailo, S. Fritzsche, P. O'Keeffe, and M. Meyer, J. Phys. B **38**, 2545 (2005).
[89] P. O'Keeffe, E. V. Gryzlova, D. Cubaynes, G. A. Garcia, L. Nahon, A. N. Grum-Grzhimailo, and M. Meyer, Phys. Rev. Lett. **111**, 243002 (2013).
[90] V. L. Jacobs, J. Phys. B **5**, 2257 (1972).
[91] K. T. Taylor, J. Phys. B **10**, L699 (1977).